Highly Sensitive Triple-Band THz Metamaterial Biosensor for Cancer Cell Detection

Ahmed Refaat Elhelw, Mahmoud Salman S. Ibrahim, Ahmed Nabih Zaki Rashed, Abd El-Naser A. Mohamed, Mohamed Farhat O. Hameed, *Senior Member, IEEE*, and Salah Sabry Ahmed Obayya, *Fellow, IEEE*

***Abstract*—Highly sensitive triple-band metamaterial-based biosensor for different cancer cells detection is suggested and numerically analyzed. The reported sensor has a polyimide dielectric layer which is sandwiched between gold bottom plane and top metallic patches. The analyte sample covers the metallic patch where multiple resonances occur with high absorption. The resonance frequencies depend on the optical properties of the analyte sample. Therefore, the proposed sensor can distinguish between different cancer cell types such as skin cancer, blood cancer, and Breast cancer. Full vectorial finite element method is used to study the effects of the geometrical parameters with the aim to maximize the sensor sensitivity. The suggested sensor has high sensitivity of 2050 GHz/RIU (which is much higher than those suggested in the literature) with high quality factor of 55.34 in the frequency range from 4.25 THz to 4.75 THz. Further, the proposed biosensor is a label-free, and easy for fabrication using the state-of-the-art fabrication technologies.**

***Index Terms*—Terahertz sensor, triple-band, cancer cell biosensor, metamaterial biosensor, plasmonics.**

Manuscript received 22 August 2023; revised 25 October 2023; accepted 3 November 2023. Date of publication 7 November 2023; date of current version 6 December 2023. This work was supported by Science, Technology and Innovation Funding Authority (STIFA) in Egypt under Project 45702. *(Corresponding authors: Salah Sabry Ahmed Obayya; Mohamed Farhat O. Hameed.)*

Ahmed Refaat Elhelw is with the Department of Electronics and Communications Engineering, Higher Institute of Engineering and Technology in Arish, Arish 45511, Egypt.

Mahmoud Salman S. Ibrahim is with the Physics Department, Faculty of Science, Arish University, Arish 45511, Egypt.

Ahmed Nabih Zaki Rashed is with the Electronics and Electrical Communications Engineering Department, Faculty of Electronic Engineering, Menoufia University, Menouf 32951, Egypt.

Abd El-Naser A. Mohamed is with the Electronics and Electrical Communications Engineering Department, Faculty of Electronic Engineering, Menoufia University, Menouf 32951, Egypt, and also with the Department of Electronics and Communications Engineering, Higher Institute of Engineering and Technology in Arish, Arish 45511, Egypt.

Mohamed Farhat O. Hameed is with the Centre for Nanotechnology, Giza 12578, Egypt, also with the Nanotechnology and Nanoelectronics Engineering Program, Zewail City of Science and Technology, and Innovation, Giza 12578, Egypt, and also with the Mathematics and Engineering Physics Department, Faculty of Engineering, University of Mansoura, Mansoura 35516, Egypt (e-mail: mfarahat@zewailcity.edu.eg).

Salah Sabry Ahmed Obayya is with the Centre for Photonics and Smart Materials, Zewail City of Science and Technology, and Innovation, Giza 12578, Egypt, and also with the Department of Electronics and Communications Engineering, Faculty of Engineering, University of Mansoura, Mansoura 35516, Egypt (e-mail: sobayya@zewailcity.edu.eg).

Digital Object Identifier 10.1109/JPHOT.2023.3330930

I. Introduction

METAMATERIAL based biosensor in THz spectrum meets the increasing request on detection and distinguishing different cancer cells in the human biological tissues. Metamaterials are engineered materials consisting of periodically arranged unit cells that are sub-wavelength dimensions. This unit cell consists of a layer of dielectric material sandwiched between the metallic ground and upper metallic patches. Metamaterials are designed to obtain unique electromagnetic properties such as perfect absorbers [1], [2], [3], solar cells [4], [5], polarization control [6], [7], and sensors [8], [9]. Tiny changes in the surroundings of the metamaterial sensor cause a variation in the electromagnetic response like optical absorption and resonance frequency. This is due to the confinement of the electric and magnetic fields on the surface of the metamaterial resonator [10]. Therefore, metamaterial sensor can be used efficiently for sensing applications such as refractive index sensor [8], cancer cell sensor [9], and chemical sensor [11].

According to the International Agency for research on cancer (IARC) statistical reports, globally the second most common cause of mortality is cancer where 36 types of cancer exist in 185 countries [12], [13]. There are numerous methods for identifying cancer cells in biological tissues and organs. The electrochemical method has a shortage of specificity in the cancer cells and paucity in the detection of intracellular protein markers [14]. Further, histopathological, or immunological methods mostly include sophisticated operation procedures, expensive, significant false positive results, and experienced personnel is highly needed [14]. In addition, other detection techniques such as fluorescence imaging, and cytometry need high costs, and long operation time [15]. However, surface plasmon resonance-based metamaterial sensors have more advantages such as high precision, label-free detection, real-time measurement, and minimal sample is needed. Azab et al. [16] have presented an overview of optical biosensors for early cancer detection including metamaterial sensors. In this context, an octagonal metamaterial ring has been presented for cancer cell detection [9] with a high sensitivity of 1649.8 GHz/RIU, and a reasonable quality factor of 11.33 at 3.15 THz. Manikandan et al. [11] have suggested dual-band metamaterial cancer cell sensor with a maximum sensitivity of 196.5 GHz/RIU, quality factor (Q) of 165, and figure of merit (FOM) of 19.65 RIU^{-1}. Further, Geng et al. [17] have presented a micro-ring metamaterial resonator integrated with microfluidics

for liver cancer biomarkers detection with a maximum frequency shift of 14 GHz at 0.025 μg/ml. Banerjee et al. [18] have proposed two circular ring resonators metamaterial as a biosensor for cancerous cells with high sensitivity of 1500 GHz/RIU, and a FOM of 25 RIU^{-1}. Vafapour et al. [19] have reported a water based biological sensor for colon cancer detection. Additionally, a graphene-based metamaterial sensor has been implemented for different types of cancer cells with a sensitivity of 207 GHz/RIU, a quality factor of 13, and FOM of 3.86 RIU^{-1} [20]. Further, a hyperbolic metamaterial sensor has been suggested for cancer cell detection with a maximum sensitivity of 500 nm/RIU ($\approx 6\times10^6$ GHz/RIU), and FOM of 85 RIU^{-1} [21]. Further, a tunable metamaterial sensor based on graphene has been presented for cancer cell detection with a sensitivity of 1100 GHz/RIU, a quality factor of 25.8, and FOM of 12.5 RIU^{-1} [22]. Askari et al. [23] have suggested a THz metamaterial refractive index sensor with a sensitivity of 7000 nm/RIU ($\approx$4.28$\times$104 GHz/RIU) and a high-quality factor of 3052.75. Moreover, Askari et al. [24] have presented a highly sensitive metamaterial sensor with a sensitivity of 4077.2 nm/RIU ($\approx$7.35$\times$104 GHz/RIU) in the frequency range of 150-500 THz. Bhati and Malik [25] have proposed a metamaterial sensor for cancer cell detection with a sensitivity of 1462 GHz/RIU. Ma et al. [26] have also suggested a highly sensitive refractive index metamaterial sensor with a sensitivity of 2372 GHz/RIU. Further, Upender and Kumar [27] have proposed a graphene metamaterial biosensor with a sensitivity of 2200 GHz/RIU. Anwar et al. [28] have presented a refractive index metamaterial sensor with a sensitivity of 1200 GHz/RIU.

The metamaterial sensors can be fabricated with conventional photolithography [5], basic chemical etching [29], and ultrashort laser machining technique [15]. Moreover, the spin coating technique followed by femtosecond laser writing can be utilized for metamaterial fabrication [30], and surface micromachining process [31]. Furthermore, the metallic patches can be thermally deposited on the dielectric layer using chemical vapor deposition (CVD) technique [29].

In this work, a highly sensitive triple-band metamaterial biosensor for different cancer cell detection is designed and analyzed numerically using the finite element method [32] via COMSOL Multiphysics simulation software package [33]. The proposed biosensor consists of a polyimide dielectric layer sandwiched between the bottom gold layer and the upper gold patch on the dielectric top surface. The gold patches are in the form of four small crosses located at the corner of a large metallic cross. Therefore, triple absorption bands are obtained due to the multiple resonators with different shapes and size [34]. Further, our proposed sensor is different from that reported in [9], [11] in design geometry and performance. The suggested design has a larger sensitivity than 1649.8 GHz/RIU presented by Azab et al., [9] that is based on octagonal two concentric rings.

In this study, sensor sensitivity, (S), quality factor, (Q), and figure of merit, (FOM) are calculated to show the performance of the suggested design. The geometrical dimensions are optimized to maximize the sensor's performance parameters. The suggested sensor has high sensitivity, S, of 2050 GHz/RIU, high-quality factor, Q, of 55.34, high FOM of 25.24 RIU^{-1}, and

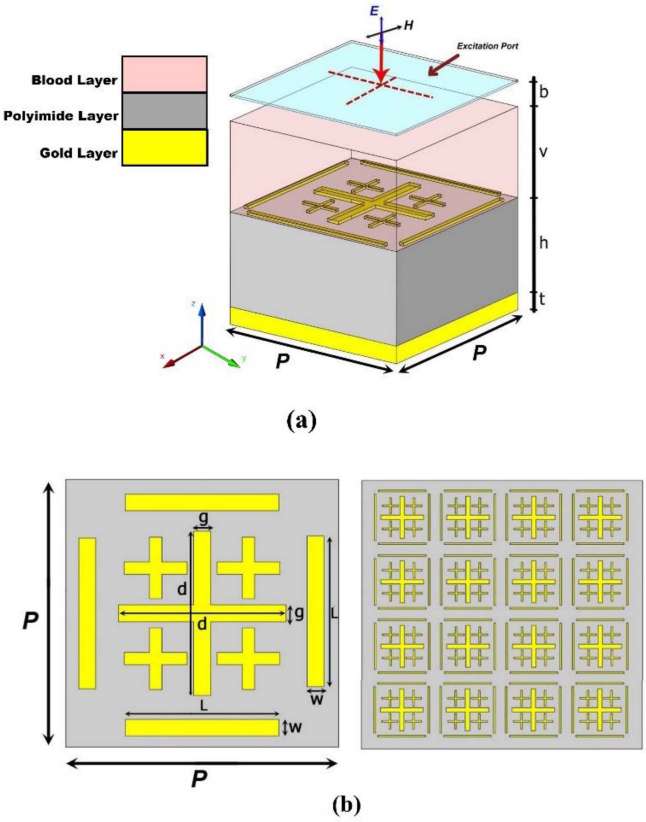

Fig. 1. (a) 3D view and (b) top view of the unit cell of the suggested sensor. The inset shows the periodic patch array of the proposed design.

absorption coefficient of 0.94132 in the range from 4.25 THz to 4.75 THz with simple and free-label design. The proposed sensor has higher sensitivity, quality factor, and FOM than those reported in [9], [20], [22], [31], [53], [62], [63], [64], [65], [18], and [68].

II. Design Considerations and Sensor Performance Parameters

The schematic diagram of the suggested metamaterial sensor is shown in Fig. 1. The unit cell has a dimension of 50 μm $\times$ 50 μm and consists of three layers as shown in Fig. 1(a). The polyimide dielectric layer with a complex dielectric constant of 2.88-0.09i [9], and thickness, $h = 4$ μm is sandwiched between the gold ground plane and top patches.

It is worth noting that the gold conductivity is nearly constant in the THz range from 0.1 THz to 4.20 THz as reported by Squires et al. [35], Choi et al. [36], and Takano et al. [37]. Therefore, the gold conductivity is taken as a constant value of 4.09×10^7 S/m in the frequency range 3.85 THz–4.1 THz as reported in [8], [9], [38], [39], [40], [41].The bottom layer has a thickness of $t = 200$ nm which is larger than the gold skin depth in the THz spectrum. Therefore, zero transmission will be obtained through the ground plane [9]. In addition, the gold patches on the top surface of the dielectric are in the form of four small crosses with a length of 7 μm, and a width of 1 μm.

TABLE I
PERFORMANCE OF THE OPTIMIZED METAMATERIAL SENSOR WITH DIFFERENT CANCER CELL TYPES [9]

Cell name	State	Sensitivity, S GHz/RIU	Quality Factor, Q	Figure of Merit, FOM, RIU^{-1}	Absorption coefficient
Basal, skin cell	Normal, n= 1.360	2050	55.34	25.24	0.94132
	Cancer, n=1.380				
Jurkat, blood cell	Normal, n=1.376	2000	54.02	24.19	0.94254
	Cancer, n=1.390				
HeLa, cervical cell	Normal, n=1.368	2000	53.33	23.85	0.94278
	Cancer, n=1.392				
PC-12, Adernal Gland cell	Normal, n=1.381	2000	53.76	25.24	0.94313
	Cancer, n=1.395				
(MDA)-(MB)-231, Breast cell	Normal, n=1.385	1928.57	52.63	22.81	0.94365
	Cancer, n=1.399				
MCF-7, Breast cell	Normal, n=1.360	2000	53.76	25.24	0.94313
	Cancer, n=1.401				

These four crosses are located at the corner of a large central cross of length $d = 25$ μm, and width of $g = 6$ μm as shown in Fig. 1(b). Moreover, the four rectangular gold metal side-stripes have a length of $L = 35$ μm, and width $w = 6$ μm. The periodic array of the proposed sensor consists of 4 × 4-unit cells with a lattice constant of P as shown in Fig. 1(b). The blood sample will cover the top surface of the metallic patches with thickness $v = 8$ μm. Further, the incident electromagnetic beam has TE polarized mode with normal incidence. However, the excitation port position is on the top surface of the sensor, i.e., $b = 0$. Firstly, the proposed sensor has been studied for skin cells with normal and basal cancer states while the refractive indices for different cell types are presented in Table I. The geometrical parameters are initially chosen for the ease of fabrication inspired from the fabricated metamaterial sensors presented in [42].

The absorption coefficient and E_z component of the electric field distribution are studied to better understand the physical interpretation of the proposed design is made by using the finite element method via COMSOL Multiphysics software package [32]. The 3D computational unit cell is discretized with a minimum element size of 7.2 nm into 427299 tetrahedral domain elements, 51706 boundary elements, and 1864 edge elements using non-uniform mesh. Furthermore, perfect electric and magnetic conductor boundary conditions are added at the opposite boundaries. In addition, impedance boundary, and transition boundary conditions have been used on the ground plane, and top metal patches, respectively. Further, the absorption coefficient proposed design is obtained using [9]:

$$A = 1 - (R + T) \tag{1}$$

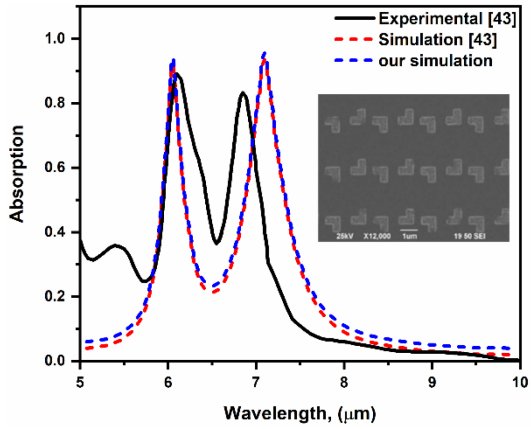

Fig. 2. Comparison between the measured and calculated wavelength-dependent absorptions of the metamaterial absorber reported in [43] and our calculations. The inset figure shows a schematic diagram of the fabricated design [43].

where R ($= S_{11}^2$) is the reflection coefficient, and T ($= S_{21}^2$) is the absorption coefficient. The transmission coefficient is zero through the analysis because of the existence of the ground gold layer.

The sensor performance is calculated in terms of the sensitivity that is given by [10]:

$$S = \frac{\Delta f}{\Delta n} \tag{2}$$

where Δf is the shift in the resonance frequency, and Δn is the change in the analyte refractive index. Additionally, the quality factor of the reported sensor is calculated [10]:

$$Q = \frac{f}{FWHM} \tag{3}$$

where f is the resonance frequency, and FWHM is the full width at half maximum bandwidth of the absorption peak. The last factor is the figure of merit that is taken as [10]:

$$FOM = \frac{S}{FWHM} \tag{4}$$

In order to prove the accuracy of our results, a comparative study is made with the simulated and experimentally measured absorption spectrum of the metamaterial absorber presented in [43]. It may be seen from this figure that a good matching between our calculations and those reported in [43] which ensures the high accuracy of our model. The simulated resonance frequency in [43] is 7.093 μm which coincides with our calculation. Therefore, our model's sensitivity calculation is expected to exhibit high accuracy. It may be also seen from Fig. 2 that there is some deviation between the simulated and fabricated results. This may be due to the assumption of the infinite array in the simulation results using periodic boundary conditions. Further, the fabricated L-shaped resonator has imperfect edges as shown in the inset of Fig. 2.

The fabrication of the proposed sensor can be made using state-of-the-art technology. First, the background gold layer with a thickness of up to 200 nm can be deposited onto a GaAs or silicon wafer through e-beam evaporation [44]. Next, the liquid

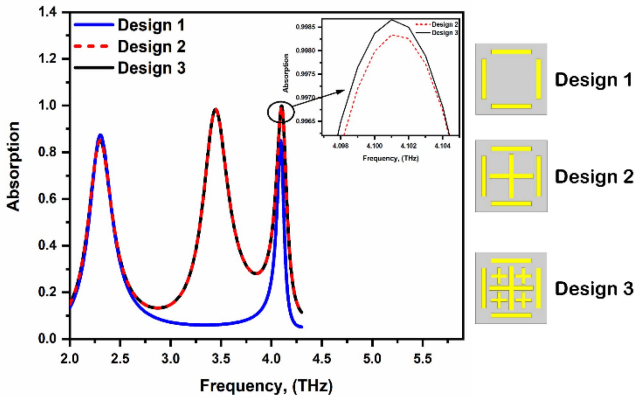

Fig. 3. Absorption spectrum for different absorber designs where the analyte sample has n = 1.36.

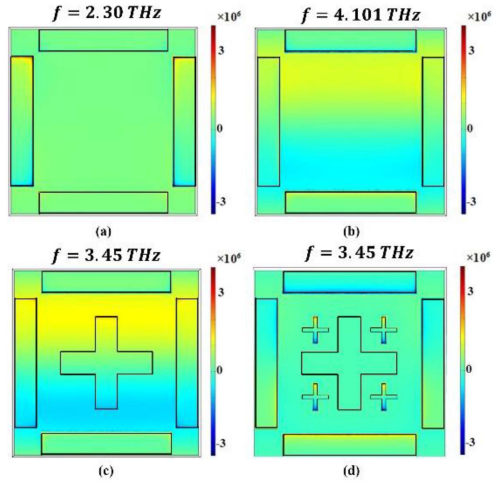

Fig. 4. Electric field distributions in the xy plane of the unit cell at (a) first resonance frequency f = 2.30 THz, (b) the third resonance frequency f = 4.101 THz, and (c), (d) the second resonance frequency of f = 3.45 THz for normal basal cell with n = 1.36.

polyimide will be deposited onto the top surface of the gold layer by spin-coating. Then, it will be heated to 110 °C for 6 minutes on a hot plate as suggested in [25], [45]. It should be next cured for five hours in an oven at 275 °C in a nitrogen environment to form the dielectric layer with thickness ranges from 0.5 μm to 8.5 μm [25], [45]. Another gold layer is deposited on the top surface of the polyimide layer via e-beam evaporation. Further, the photoresist layer is deposited on the top dielectric layer with spin coating and the patterns will be transferred from a photomask to the photoresist via UV exposure and developed within AZ300 MIF. The photolithography may be also used to obtain the metallic patches. In addition, excess gold will be removed by ion beam etching, and the photoresist will be cleaned with acetone. The analyte sample covers the top surface of the sensor using a micropipette. Finally, the time domain THz spectrometer in the range from 0.1 THz–6 THz with a reflection setup can be used to characterize the proposed sensor [38], [46], [47]. Therefore, it is believed that our reported structure can be fabricated successfully.

Fig. 3 shows the absorption spectrum for design 1 with rectangular metallic stripes, design 2 with rectangular metallic stripes with large central cross, and design 3 with additional small crosses. The absorption spectrum is obtained for normal basal cells with n = 1.36 on the surface of the sensor [9]. It may be seen that for design 1, two resonance peaks are obtained at f = 2.30 THz and 4.101 THz with the absorption coefficient of 0.8504 this resonance frequency is due to the electric dipole between the vertical and horizontal outer rectangular strips with the ground gold layer, respectively as shown in Fig. 3. In addition, for design 2, a third resonance peak is achieved at f = 3.45 THz owing to the electric dipole between the cross shape and the background layer as shown in Fig. 3. Further, the absorption coefficient of the third band is enhanced from 0.8504 to 0.9987 from design 1 to design 2. It is also evident that design 2, and design 3 achieve high absorption coefficient for the third resonance peak. However, design 3 has a better FOM and Q factor with enhancement factors of ≈11.43% (from 16.09 for Design 2 to 17.93 for Design 3), and ≈8.6% (from 32.85 for Design 2 to 35.70 for Design 3) for the FOM and quality factor, respectively. Further, Design 3 has a higher absorption coefficient and as a result, a higher quality factor than Design 2 because Design 3 achieves better impedance matching with free space than Design 2. The high-quality factor and FOM are highly needed for accurate sensor's performance. Therefore, design 3 is considered for the proposed sensor [9].

Fig. 4 shows the electric field distributions in the x-y plane, at the three resonance frequencies of 2.30, 3.45, and 4.101 THz, respectively. As shown in Fig. 4(a), the electric field is concentrated on the outer vertical rectangular strips and their edges, indicating strong electrical resonance. Therefore, the first absorption peak at f = 2.30 THz is excited by the outer vertical rectangular stripe resonator. In addition, Fig. 4(b) shows that at the third resonance frequency, at f = 4.101 THz, the electric field is mainly focused on the outer horizontal rectangular strips and their edges, indicating strong electrical resonances. However, at the resonance frequency f = 3.45 THz, the electric field is distributed primarily on the inner cross-shaped resonators and their edges, as shown in Fig. 4(c) and (d), [48].

III. Sensitivity Analysis for Cancer Early Detection

The proposed design has triple-absorption bands as shown in Fig. 5(a) for normal basal cell (n = 1.36) and basal cancerous cell (n = 1.38). The first band with resonance frequency at f = 2.30 THz for normal cells, and 2.29 THz for basal cancer cells with sensitivity of 500 GHz/RIU and maximum absorption coefficient of 0.85223. The second resonance occurs at f = 3.45 THz for normal cells and 3.43 THz for basal cancer cell with sensitivity of 1000 GHz/RIU and absorption coefficient of 0.9839. The third band resonates at f = 4.101 THz and 4.061 THz for both normal and basal cancer cells, respectively with a sensitivity of 2000 GHz/RIU. Therefore, the third band is more sensitive to the variation in the refractive index of the analyte samples and is chosen for the consequent studies.

The reported sensor has a high sensitivity of 2000 GHz/RIU, a high-quality factor of 35.70, FOM of 17.93 RIU^{-1} using the initial geometrical parameters. According to the impedance matching theory, the impedance of the perfect absorption design

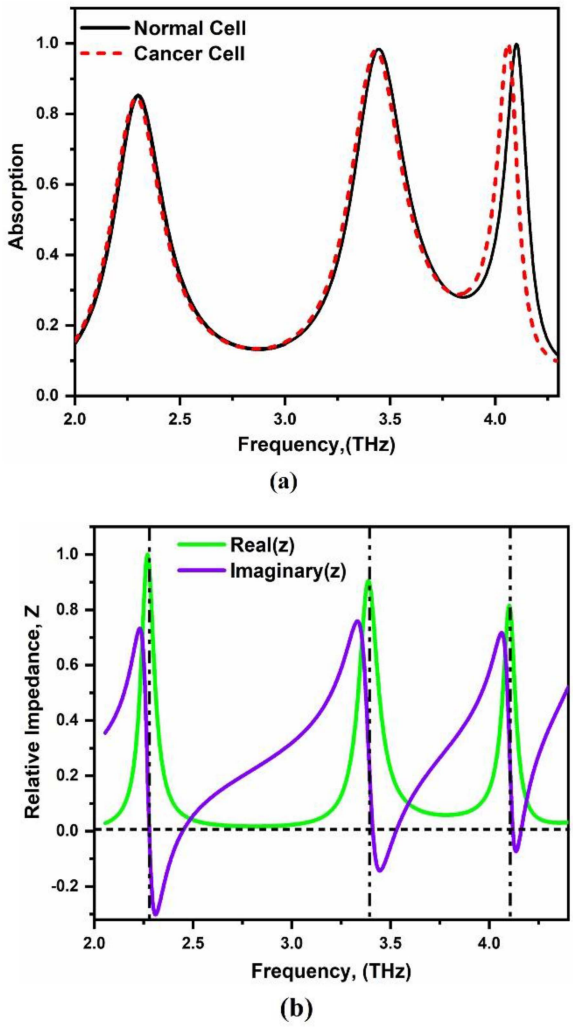

Fig. 5. (a) Triple THz bands for the proposed sensor at initial geometrical values for normal and basal cancerous cells, (b) the real part and imaginary part of the relative impedance for the triple resonance peaks for normal basal cell with n = 1.36.

should be matched with the free space impedance as much as possible in order to reduce the reflection from the surface of the proposed design [39]. The relative impedance of the proposed sensor is given by [49]:

$$Z = \pm\sqrt{\frac{(1+S_{11}(\omega))^2 - S_{21}^2(\omega)}{(1-S_{11}(\omega))^2 - S_{21}^2(\omega)}} \tag{5}$$

Fig. 5(b) shows the real and imaginary parts of the relative impedance for the triple band of the proposed design using a normal cell. It may be seen that at the resonance frequencies, the real part and imaginary part of the relative impedance are very close to 1, and zero, respectively. The relative impedance is 0.463–0.296i for the first resonance peak, 0.583–0.121i for the second resonance peak, and 0.798+0.00618i for the third resonance peak which confirms the high absorption coefficients of the resonance frequencies with low reflection.

The shift in the resonance peaks for normal and cancerous cells shown in Fig. 5(a) may be interpreted using equivalent circuit theory as given by [10]:

$$f = \frac{1}{2\pi\sqrt{L_{eq}C_{eq}}} \tag{6}$$

where f is the resonance frequency, $L_{\rm eq}$, and $C_{\rm eq}$ are the equivalent inductance and capacitance of the sensor. The refractive index of the analyte increases from 1.36 to 1.38 for normal and basal cancer cells. Therefore, the equivalent capacitance of the analyte increases. Additionally, the resonance frequency is inversely proportional to the square root of the analyte capacitance. Hence, the resonance frequency is red-shifted with the increase of the analyte refractive index [10]. Also, the first-order electromagnetic perturbation theory can be used to interpret the red shift of the resonance frequency as the refractive index of the analyte increases [50]. The electric field as shown in Fig. 4(d) is well confined around the edges of the metallic crosses with an ultrahigh absorption coefficient of 0.9987. The field distribution points out the aggregation of opposite charges near the edges of the crosses for the excited surface plasmon polariton resonance (SPR) mode which is the main source of light absorption [51]. In addition, the negative charges are concentrated at the top horizontal rectangular metal side stripe while the positive charges are concentrated at the bottom horizontal strip which acts as an electric dipole that also attributes in the absorption [38], [52]. Therefore, the total absorption is based on the coupling between electric dipole and surface plasmon resonance [52].

In order to enhance the sensor performance, parametric sweep studies are made on the different geometrical parameters including, rectangular side-stripes, large central cross, lattice constant of the periodic array, thickness of the dielectric layer, and thickness of the analyte layer. First, the effect of the width of the four rectangular side stripes on the absorption performance, sensitivity, and quality factor is shown in Fig. 6. However, the other geometrical parameters are kept constant at their initial values. Fig. 6(a) shows that at $w = 1.0$ μm, the obtained sensitivity is equal to 2300 GHz/RIU. Further, it is revealed from Fig. 6(a) that the resonance frequency decreases as the rectangular side-stripe width increases. This is because of the increase in the equivalent inductance and capacitance of the proposed sensor as the stripe width increases. Accordingly, the resonance frequency decreases [29], [51]. In Fig. 6(b), it is revealed that the quality factor decreases as the stripe width increases. This is due to the decrease of the radiation losses (absorption increases from 0.89349 at w = 1 μm to 0.99992 at w = 6 μm) [51]. Fig. 6(b) also clarifies that the obtained sensitivity is 2300 GHz/RIU at w = 1 μm. then, it is increased to 2350 GHz/RIU at w = 3 μm. As the rectangular stripe width is further increased from 3 μm to 6 μm, the sensitivity decreases from 2350 GHz/RIU to 2000 GHz/RIU. Therefore, the optimum sensitivity has a value of 2350 GHz/RIU with a high-quality factor of 54.59, and FOM of 31.12 RIU^{-1} at the optimum stripe width, w = 3 μm with a maximum absorption of 0.9663 for the consequent analysis.

Next, the impact of the stripe length, L, is studied, while the stripe width w is kept constant at 3 μm, and the other geometrical dimensions are taken as their initial values. Fig. 7 reveals that at $L = 25$ μm, the frequency resonance is obtained at 4.157 THz,

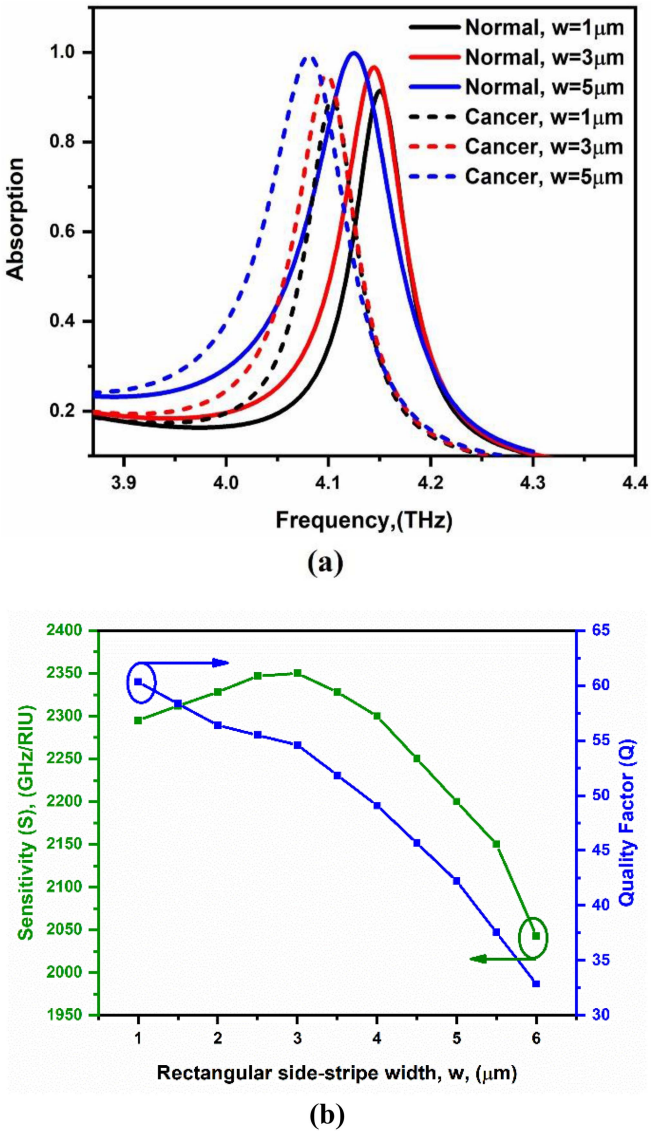

Fig. 6. (a) Absorption spectrum versus the frequency at different stripe widths, w, and (b) variation of the sensitivity and the quality factor, Q with the stripe width, w.

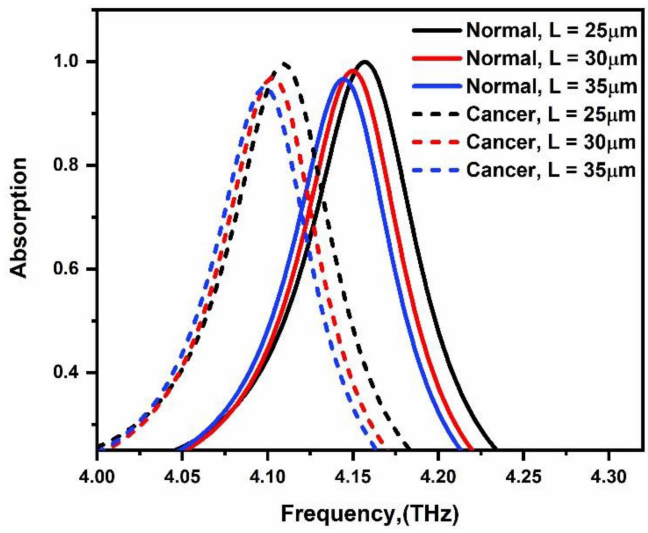

Fig. 7. Absorption spectrum versus frequency at different stripe lengths, L for normal and basal cancer cell.

and 4.109 THz for normal, and cancer Basal cells, respectively. Accordingly, the resultant frequency shift is 48 GHz with a corresponding sensitivity of 2400 GHz/RIU. When a stripe length of 30 μm is used, the resonance frequencies are shifted to 4.15 THz and 4.103 THz with a frequency shift of 47 GHz for normal and basal cancer cells, respectively. As a result, the sensitivity is decreased to 2350 GHz/RIU as shown in Fig. 7. Further, when the stripe length is $L = 35$ μm, the resonance frequencies are 4.145 THz, and 4.099 THz for normal and basal cancer cells, respectively with frequency shift of 46 GHz. Accordingly, the sensitivity is equal to 2300 GHz/RIU. Therefore, an optimum stripe length of $L = 25$ μm with a sensitivity of 2400 GHz, quality factor of 82.82, and FOM of 30.67 RIU^{-1} is chosen for the next study. It may also be seen that the resonance frequency shifts to lower values as the length of the rectangular stripe increases. As the stripe length increases, the gap between them decreases. Accordingly, the equivalent capacitance increases, and hence, the resonance frequency decreases. In addition, the absorption coefficient decreases as the stripe length increases. It is due to the relative impedance mismatching with the free space which increases with increasing the stripe length L. Hence, the reflection intensity increases with a reduced absorption coefficient [53] as shown in Fig. 8. Moreover, the decrease in the absorption coefficient can also be explained by the E_z component of the electric field distribution. Fig. 9 shows the z-component of the electric field distribution for the proposed sensor at different values of the stripe length. It is revealed that the electric field confinement decreases as the rectangular stripe length increases, and hence, the absorption coefficient decreases with increasing the stripe length. Therefore, $L = 25$ μm will be chosen for the next simulations.

In the next study, the impact of the length d of the central cross on the absorption spectrum and sensor sensitivity is obtained and shown in Fig. 10. The central cross length varies at $d = 25$, 30, and 35 μm, with optimum $w = 3$ μm, $L = 25$ μm, while the other dimensions are kept constant at their initial values. It may be seen from Fig. 10 that the resonance frequency shifts to lower values as the central cross length increases. As d increases, the gap between the cross and strips decreases. Accordingly, the equivalent capacitance increases, and hence, the resonance frequency is shifted to lower values. At $= 25$ μm, the frequency resonance is obtained at 4.157 THz, and 4.109 THz for normal, and cancer Basal cells, respectively. Accordingly, the frequency shift is 48 GHz with a corresponding sensitivity of 2400 GHz/RIU. When a stripe length of 30 μm is used, the resonance frequency is shifted to 4.145 THz and 4.098 THz for normal and basal cancer cells, respectively with a corresponding frequency shift of 47 GHz. Accordingly, the sensitivity is decreased to 2350 GHz/RIU. Further, when the stripe length is $d = 35$ μm, the resonance frequencies are 4.138 THz, and 4.092 THz for normal and basal cancer cells, respectively with a frequency shift of 46 GHz with

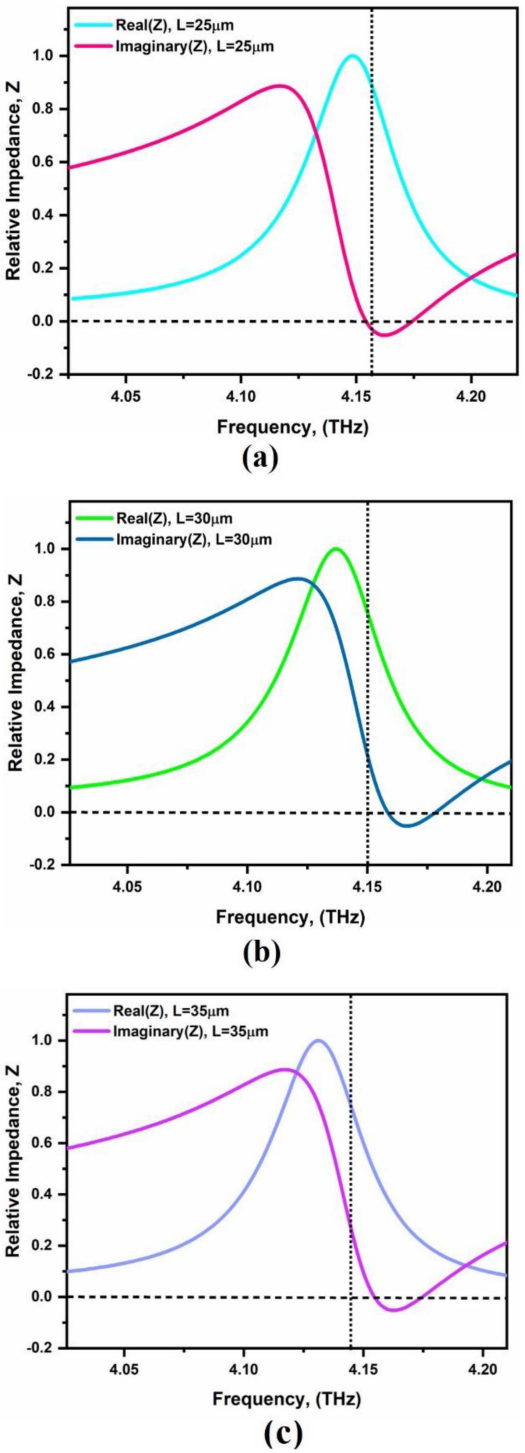

Fig. 8. Real part and imaginary part of the relative impedance for (a) L = 25 μ, (b) L = 30 μm, and (c) L = 35 μm.

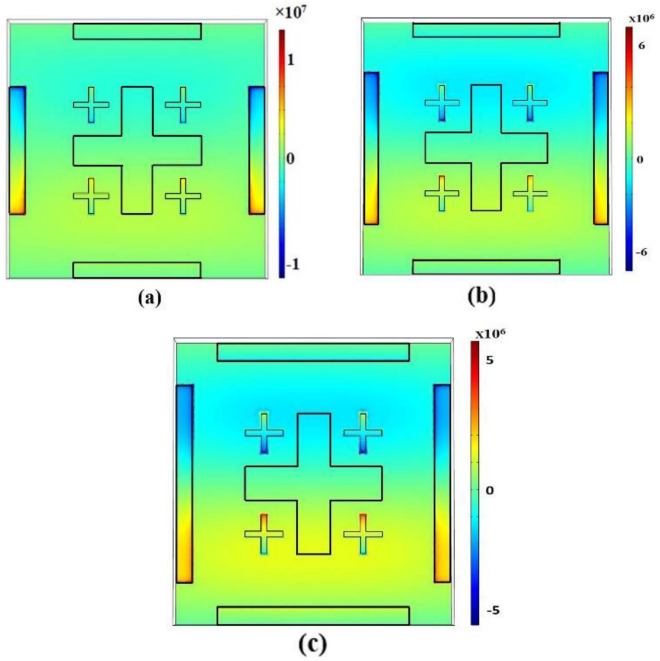

Fig. 9. E_z electric field distribution for (a) L = 25 μ, (b) L = 30 μm, and (c) L = 35 μm for normal cell of basal with n = 1.36.

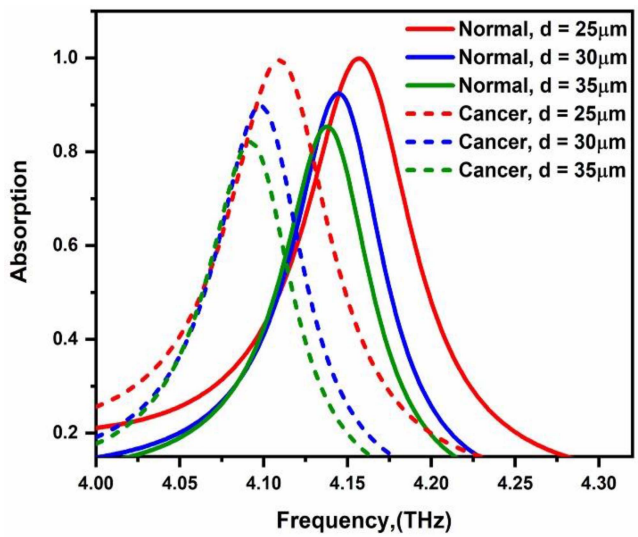

Fig. 10. Frequency dependent absorption spectrum at different values of central cross length, *d* for normal cell of basal and cancerous cells.

a sensitivity of 2300 GHz/RIU. Therefore, the optimum stripe length of $d = 25$ μm with a sensitivity of 2400 GHz, quality factor of 82.82, FOM of 30.67 RIU^{-1}, and maximum absorption coefficient of 0.999 is chosen for the next study.

The effect of the central cross width, *g* is obtained at values of 8, 9, and 10 μm as shown in Fig. 11. It is revealed that at $g = 8$ μm, the resonance frequencies are 4.161, and 4.113 THz for normal and basal cancer cells, respectively. As a result, the frequency shift is 48 GHz with a corresponding sensitivity of 2400 GHz/RIU. When the central cross width is increased to 9 μm, the resonance frequencies are 4.163 THz for normal basal cells and 4.114 THz for cancer cells with a frequency shift of 49 GHz. Therefore, a high sensitivity of 2450 GHz/RIU is obtained. As the central cross width is further increased to 10 μm, the obtained sensitivity decreases to 2400 GHz/RIU as illustrated in Fig. 11. As a result, the central cross width of g = 9 μm with sensitivity of 2450 GHz/RIU, quality factor of 46.58, FOM of

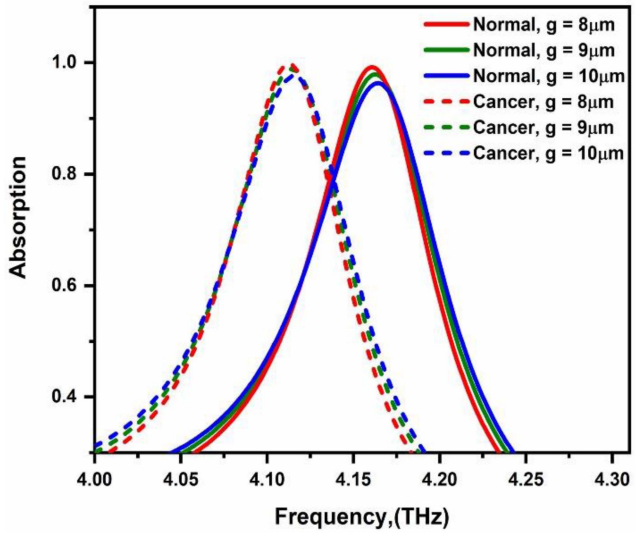

Fig. 11. Frequency dependent absorption spectrum at different central cross widths, g for normal cell of basal and cancerous cells.

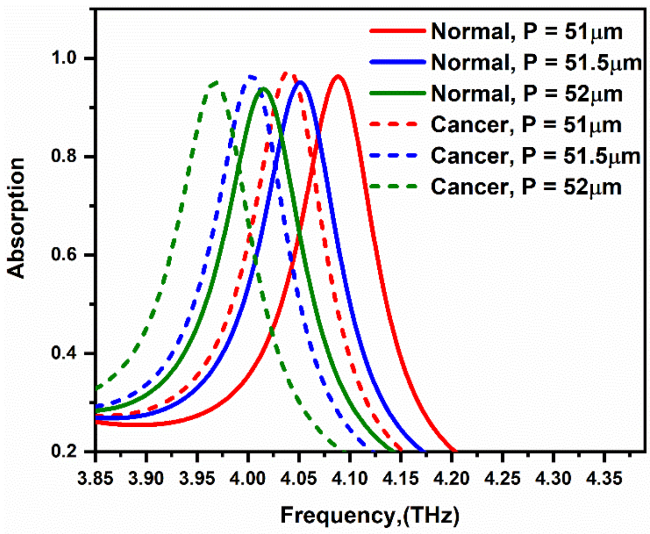

Fig. 12. Absorption spectrum versus frequency of the reported design at different periods between neighboring unit cells, P for normal and basal cancer cells.

27.62 RIU^{-1}, and maximum absorption coefficient of 0.98837 is chosen as an optimum value for the consequent study.

Next, the impact of the period, P, on the absorption spectrum, and sensor sensitivity is obtained from 51 μm to 52 μm as shown in Fig. 12. In this study, the width of the rectangular side stripes is $w = 3$ μm, with length of $L = 25$ μm, central cross length of $d = 25$ μm, and width of g = 9 μm. However, the other geometrical dimensions are kept constant at their initial values. From Fig. 12, it is revealed that as the period decreases, the multi-mode resonant coupling effect between the neighboring unit cells increases. This will increase the absorption peaks with reduced FWHM [54] as shown in Fig. 12. According to the LC circuit model, when the unit cell period increases, the gap size between neighboring unit cells will decrease. As

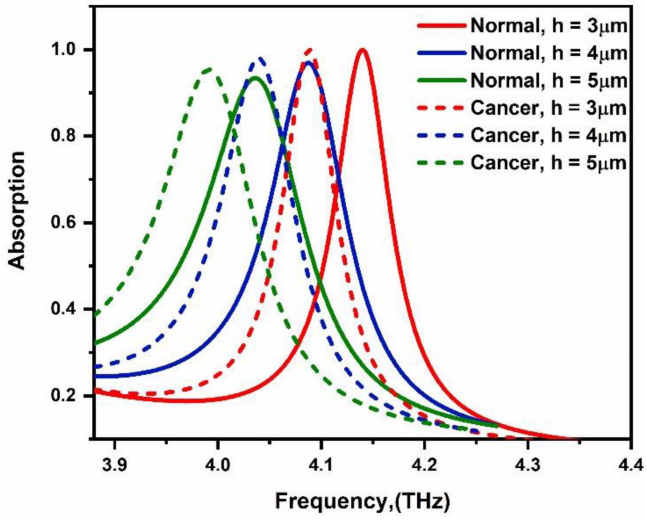

Fig. 13. Absorption spectrum versus frequency of the reported design at different dielectric layer thickness, h for normal and basal cancer cells.

a result, the capacitance between neighboring unit cells will increase. Therefore, the resonance frequency will shift to a lower value [51], [55]. Further, it is revealed that at P = 51 μm, the resonance frequencies are 4.089, and 4.040 THz for normal and basal cancer cells, respectively. Accordingly, the obtained frequency shift is 49 GHz which corresponds to a sensitivity of 2450 GHz/RIU. When the period is increased to 51.5 μm, the resonance frequencies are 4.052 THz for normal basal cells and 4.004 THz for cancer cells with a frequency shift of 48 GHz. Therefore, the obtained sensitivity is 2400 GHz/RIU. When the period is greatly increased to 52 μm, the sensitivity decreases to 2350 GHz/RIU as illustrated in Fig. 12. As a result, P = 51 μm with a sensitivity of 2450 GHz/RIU, quality factor of 41.35, FOM of 24.88 RIU^{-1}, and maximum absorption coefficient of 0.97436 is chosen as an optimum value for the next study.

The impact of the dielectric layer thickness, h, is next studied as shown in Fig. 13. It is revealed that at $h = 3$ μm, the resonance frequencies are 4.14, and 4.089 THz for normal and basal cancer cells, respectively. As a result, the frequency shift is 51 GHz which corresponds to a sensitivity of 2550 GHz/RIU. As h is increased to 4 μm, the resonance frequencies are equal to 4.089 THz for normal basal cells and 4.040 THz for cancer cells with a frequency shift of 49 GHz. Therefore, the obtained sensitivity is 2450 GHz/RIU. When the dielectric thickness is greatly increased to 5 μm, the corresponding sensitivity decreases to 2250 GHz/RIU as illustrated in Fig. 13. As a result, the dielectric thickness of $h = 3$ μm with sensitivity of 2550 GHz/RIU, quality factor of 62.02, FOM of 38.44 RIU^{-1}, and maximum absorption coefficient of 0.99981 is chosen as an optimum value for the consequent study. As the dielectric layer thickness, h increases from 3 to 5 μm, the resonant frequency and the absorption coefficient are changed. It is revealed that the absorption peak frequency is shifted to lower values as h increases. As the dielectric layer thickness h increases the equivalent inductance of the polyimide layer should be increased which decreases the equivalent capacitance between the two metallic plates. Whereas

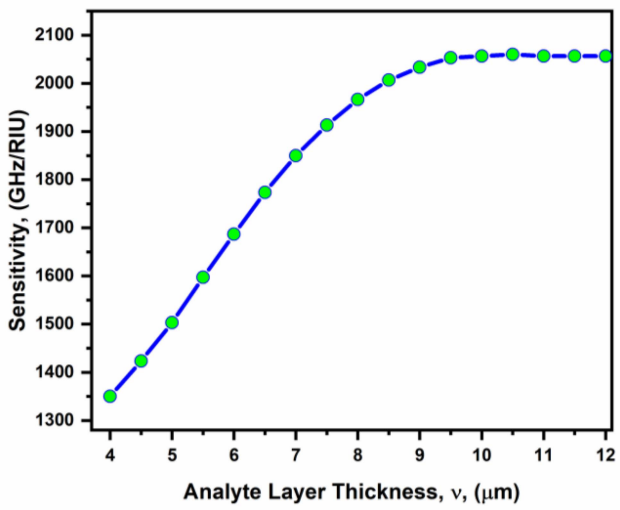

Fig. 14. Variation of the sensor sensitivity with the analyte layer thickness, v.

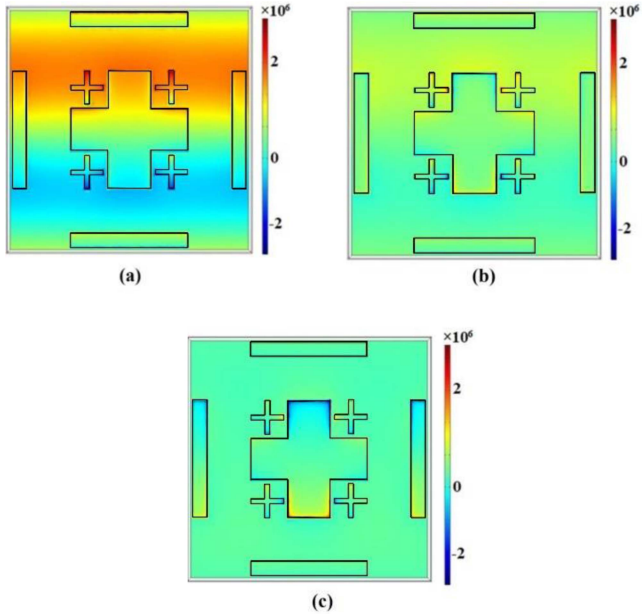

Fig. 15. Ez electric field distribution through the suggested design using analyte layer of the normal cell of basal with the thickness of (a) v = 8.5 μm, (b) v = 9 μm, and (c) v = 9.5 μm.

the decrease in the equivalent capacitance is somewhat less than the increase in the inductance, as a result, a decrease in the resonant frequency is obtained [29]. Further according to the transmission phase relation reported in [56]:

$$\alpha = \frac{4h\sqrt{\varepsilon_r - \sin^2\theta}}{\lambda} \tag{7}$$

where ε_r and λ are the dielectric constant and wavelength, respectively. The ratio h/λ remains fixed with constant values of ε_r, α, and θ. As a result, the relationship between the resonating frequency and the substrate thickness is inversely proportional. The position of the excitation port is also tested. It is found that the sensitivity has very good stability when the excitation source is located at 3.0 μm from the top surface of the proposed sensor. As a result, the corresponding sensitivity drops from 2550 GHz/RIU to 1950 GHz/RIU.

It should be noted that the polyimide dielectric thickness is suitable for the fabrication feasibility as reported in [10]. Further, Manikandan et al. [11] have reported that the polyimide thickness of 2 μm can be fabricated easily. According to Anwar et al. [40] the dielectric thickness of around 5 μm is suitable for fabrication purposes. In addition, Dai et al. [57] have reported a polyimide layer thickness of 3 μm. Huang et al. [41] have reported polyimide thickness ranges from 4 μm to 8 μm in the THz region. Moreover, based on the experimental steps for the fabrication of the proposed sensor, the polyimide can be fabricated with any thickness by using liquid polyimide spin coated and then cured in an oven for solidification as mentioned [25], [45].

Finally, the analyte thickness, v, is then studied where it varies from 4.0 μm to 11.0 μm as shown in Fig. 14. It may be seen that the sensitivity changes with increasing the analyte thickness when $v < 9$ μm and steadily achieves saturation when $v > 9$ μm. This is because the surface current on the sensor surface will be excited to oscillate by the incident wave. This is confirmed by the electric field distribution as shown in Fig. 15 with a normal

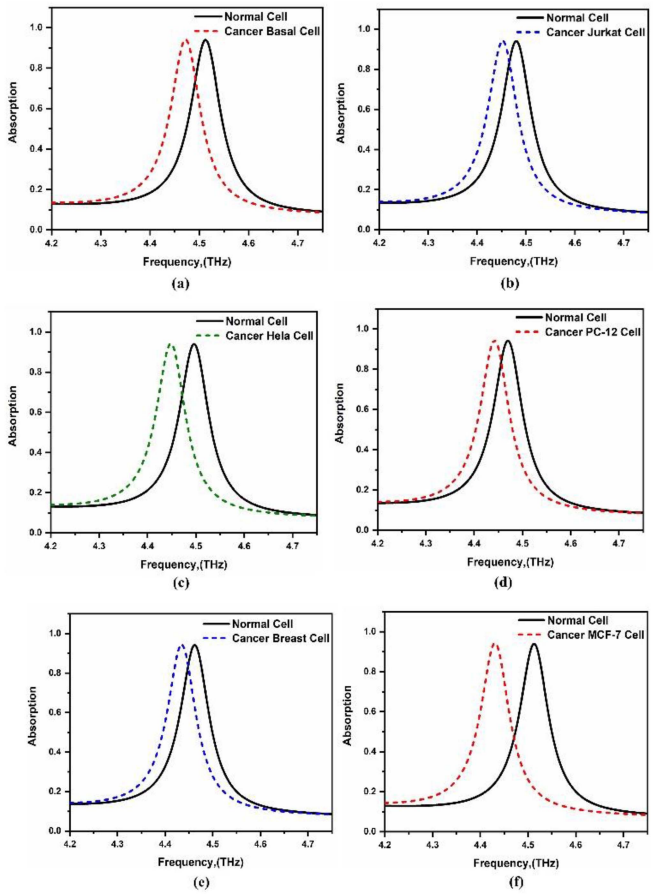

Fig. 16. Frequency-dependent absorption coefficients of the proposed design using normal and cancerous cells of different types; (a) basal, (b) jurkat, (c) HeLa, (d) PC-12, (e) breast, and (f) MCF-7.

TABLE II
IMPACT OF THE GEOMETRICAL PARAMETER'S TOLERANCE ON THE PERFORMANCE OF THE SUGGESTED SENSOR

Structure parameter	Tolerance	Sensitivity, (GHz/RIU)	Quality Factor	Figure of Merit, (RIU^{-1})	Absorption coefficient
Dielectric thickness, $h = 3\mu m$	+10%	2100	47.35	22.23	0.90376
	-10%	2100	64.71	30.12	0.97216
Analyte thickness, $v = 9\mu m$	+10%	2050	57.98	27.84	0.935647
	-10%	1950	56.52	24.43	0.94982
Lattice constant, P = 51μm	+10%	2000	55.70	24.84	0.93976
	-10%	2050	56.18	25.58	0.94282
Central cross width, $g = 9\mu m$	+10%	2000	55.15	24.53	0.91098
	-10%	2000	61.37	27.34	0.96812

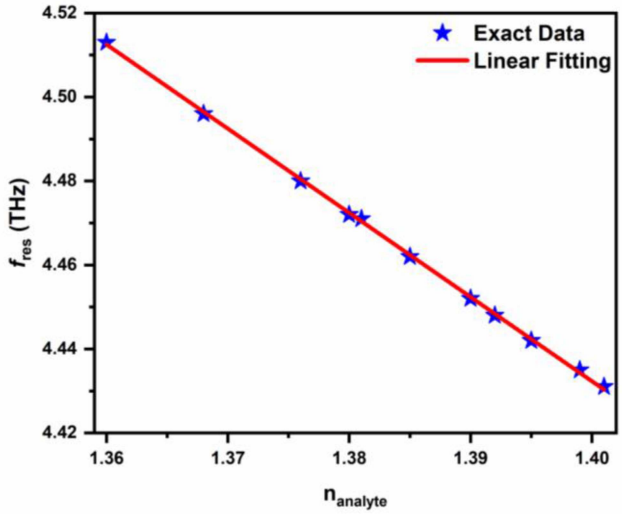

Fig. 17. Resonance frequency variation with the analyte refractive index.

cell of basal with n = 1.36. The larger the analyte thickness, the faster the attenuation of the oscillations [58]. As a result, the analyte layer thickness $v = 9$ μm is chosen for the optimized sensor. The reported sensor has a sensitivity of 2050 GHz/RIU, a quality factor of 55.34, FOM of 25.24 RIU^{-1} with a maximum absorption coefficient of 0.94132.

Table I lists the performance parameters of the suggested sensor for different types of normal and cancer cells where the absorption spectrum of each case is shown in Fig. 16. It is evident that the suggested THz metamaterial absorber can be used as a highly sensitive sensor for the detection of various types of cancer cells.

The fabrication tolerance study is also performed and presented in Table II. In this study, only one parameter is studied at a time while the others are kept constants. It is evident from this table that the proposed sensor has high reliability against fabrication faults with a tolerance of ±10% for the different geometrical parameters where a minimum sensitivity of 1950 GHz/RIU is achieved.

The linearity of the proposed metamaterial biosensor is studied with analyte refractive indices variation from $n = 1.36$ to 1.401 RIU. Fig. 17 shows the variation of the resonance frequency with the analyte refractive index using optimized geometrical dimensions. It is revealed that the suggested design

TABLE III
PERFORMANCE COMPARISON WITH THE MOST RECENT DESIGNS IN THE LITERATURE, NR: REFERS TO NOT REPORTED

Design	Analyte	Sensitivity, GHz/RIU	Quality Factor	Figure of Merit, (RIU^{-1})
Two loops of concentric hexagonal gold layers [9]	Skin cancer, Breast cancer, Blood cancer	1649.8	10.64	NR
Four Trishul structures with a cross aperture in the center [11]	Refractive index	196.5	165	19.65
Four split ring resonator structures with four gaps [20]	Skin cancer, Blood cancer, Adrenal cancer, Breast cancer, Cervical cancer	207	13	3.86
Two-layer graphene disk [22]	Breast cancer	1100	25.8	12.5
Split-resonant-rings [25]	Hepatocellular Carcinoma	68	NR	NR
Symmetry square bracket of InSb [42]	Refractive index	287	16.3	2.8
Split rings and cross combine structures [62]	Candida Albicans, E. Coli, and Shigella Dysenteriae	290	NR	NR
Asymmetric Split Square Resonator [63]	Bovine serum albumin protein	278	11	NR
Buzzle resonator incorporated with a thin graphene layer [64]	Breast cancer, Blood cancer	495	82	NR
Graphene semicircle rings [65]	Refractive index	1400	40.52	17.30
Micro-ring shaped structure GaAs [66]	Refractive index	1450	460.08	301.45
Two circular ring resonators [18]	Blood cancer, Basal cancer	1500	44	25
Split ring resonator [67]	Cervical cancer, Blood cancer, Breast cancer	658	14.93	258
Split square ring resonator [68]	Cervical cancer	74	NR	NR
asymmetrical metallic resonators [69]	Skin cancer, Blood cancer, Breast cancer, Cervical cancer	1870	456.5	125
This Work	**Skin cancer, Blood cancer, Breast cancer, Cervical cancer**	**2050**	**55.34**	**25.24**

The bold values highlight the optimized performance values for the proposed sensor for different cancer cell detection compared with that reported in literature.

has a high linearity during the studied refractive index range with an R of 0.99984. The equation of the linear fitting is expressed as:

$$f\ [THz] = -2.00467\,[THz] \times n + 7.23887 \qquad (8)$$

where n is the refractive index of the analyte and f_{res} is the corresponding resonance frequency. Accordingly, the proposed sensor can be used to detect various cancer cells early with an average sensitivity of 2004 GHz/ RIU.

It is worth noting that the cancer cells are nondispersive materials where the refractive index is nearly constant in the 1–6 THz region as reported in [59], [60], [61]. Therefore, the refractive indices of the cancerous cells are taken as shown in Table III in the frequency range of 3.85 THz–4.1 THz as reported in [9], [20], [22], [64], [18], [68], [69]. A comparison between the performance of the reported biosensor and the recently suggested THz metamaterial sensors is shown in Table III. It is revealed that the suggested sensor achieves larger sensitivity than those reported in the literature. In addition, the reported sensor has the highest quality factor, but the quality factor is lower than that presented in [11], [64], [66], [69]. In [11], the authors have suggested a high-quality factor sensor but with very low sensitivity and figure of merit. Also, the authors in [66] have presented a refractive index sensor with high-quality factor and FOM but with low sensitivity compared to our design. Further, the proposed sensor achieves a higher FOM than that suggested in the literature. But it is lower than that reported in [66], [67], and comparable with that proposed in [18]. Thus, our proposed work provides a high-performance design with high sensitivity, high-quality factor, and a FOM with a simple design. Furthermore, the proposed metamaterial-based biosensor sensitivity is also larger than that of the recently developed PCF biosensors for cancer cell detection. PCF-based biosensors have some drawbacks like coupling losses, and mode conversion because they rely on excitation of the fundamental mode, and the high cost of fabrication with complex design [9].

IV. Conclusion

In this work, a highly sensitive metamaterial-based biosensor for various types of cancer cell detection is studied and numerically analyzed. The suggested design is based on a large central gold cross with four small crosses in the corner, surrounded by four gold rectangular side strips which achieves a high absorption coefficient value > 0.94 with a high-quality factor of 55.34. Moreover, the implementation of the proposed design in cancer cell detection results in a very high sensitivity of 2050 GHz/RIU with a FOM of 25.24 RIU^{-1} for basal type. Further, an average sensitivity of 2000 GHz/RIU has been obtained for other types of cancer which is higher than that reported in the recent literature [9], [11], [20], [22], [31], [53], [62], [63], [64], [65], [66], [18], [67], [68], [69].

Further, the performance of the proposed design has high reliability with a fabrication tolerance of $\pm 10\%$ for the different geometrical parameters where high sensitivity is achieved. Furthermore, the fabrication of the proposed sensor can be recognized with state-of-the-art technologies that have been used in fabricating devices with similar designs. Therefore, the proposed biosensor is efficient in early detection of different cancer cells with a simple design and label-free technique.

Reference

[1] G. Y. Abdelatif, M. F. O. Hameed, S. S. A. Obayya, and M. Hussein, "Ultrabroadband absorber based on a funnel-shaped anisotropic metamaterial," *J. Opt. Soc. Amer. B*, vol. 36, no. 10, pp. 2889–2895, 2019, doi: 10.1364/JOSAB.36.002889.

[2] G. Y. Abdel-Latif, M. F. O. Hameed, and S. S. A. Obayya, "Thermal absorber with epsilon-near-zero metamaterial based on 2D square spiral design," *J. Opt. Soc. Amer. B*, vol. 38, no. 12, pp. 3878–3885, 2021, doi: 10.1364/JOSAB.425856.

[3] H. Hamdy, G. Y. Abdel-Latif, M. El-Agamy, H. A. El-Mikati, M. F. O. Hameed, and S. S. A. Obayya, "Wavelength-selective metamaterial absorber based on 2D split rhombus grating for thermophotovoltic solar cell," *Opt. Quantum Electron.*, vol. 54, no. 2, pp. 1–12, 2022, doi: 10.1007/s11082-021-03459-w.

[4] R. Kumar, B. K. Singh, and P. C. Pandey, "Broadband metamaterial absorber in the visible region using a petal-shaped resonator for solar cell applications," *Phys. E Low-Dimensional Syst. Nanostructures*, vol. 142, 2022, Art. no. 115327, doi: 10.1016/j.physe.2022.115327.

[5] Y. C. Chao et al., "Unconventional organic solar cell structure based on hyperbolic metamaterial," *J. Mater. Chem. C*, vol. 11, no. 6, pp. 2273–2281, 2023, doi: 10.1039/d2tc04723c.

[6] M. A. A. Abouelatta, S. S. A. Obayya, and M. F. O. Hameed, "Highly efficient transmissive metasurface for polarization control," *Opt. Quantum Electron.*, vol. 53, no. 2, pp. 1–11, 2021, doi: 10.1007/s11082-020-02697-8.

[7] V. A. Seyfi, A. E. Gayduk, and V. Y. Prinz, "Tunable chiral metamaterial for polarization control in microwave region," in *Proc. IEEE 21st Int. Conf. Young Specialists Micro/Nanotechnol. Electron Devices*, 2020, pp. 64–67, doi: 10.1109/EDM49804.2020.9153342.

[8] A. S. Saadeldin, M. F. O. Hameed, E. M. A. Elkaramany, and S. S. A. Obayya, "Highly sensitive terahertz metamaterial sensor," *IEEE Sensors J.*, vol. 19, no. 18, pp. 7993–7999, Sep. 2019, doi: 10.1109/JSEN.2019.2918214.

[9] M. Y. Azab, M. F. O. Hameed, A. M. Nasr, and S. S. A. Obayya, "Highly sensitive metamaterial biosensor for cancer early detection," *IEEE Sensors J.*, vol. 21, no. 6, pp. 7748–7755, Mar. 2021, doi: 10.1109/JSEN.2021.3051075.

[10] M. R. Nickpay, M. Danaie, and A. Shahzadi, "Graphene-based tunable quad-band fan-shaped split-ring metamaterial absorber and refractive index sensor for THz spectrum," *Micro Nanostructures*, vol. 173, 2023, Art. no. 207473, doi: 10.1016/j.micrna.2022.207473.

[11] E. Manikandan, K. A. Karthigeyan, A. Arivarasi, and E. Papanasam, "High-Q and FOM dual-band polarization dependent ultra-narrowband terahertz metamaterial sensor," *IEEE Photon. J.*, vol. 15, no. 1, Feb. 2023, Art. no. 0600206, doi: 10.1109/JPHOT.2023.3234074.

[12] [Online]. Available: https://gco.iarc.fr/today/home

[13] R. L. Siegel, K. D. Miller, N. S. Wagle, and A. Jemal, "Cancer statistics, 2023," *CA Cancer J. Clin.*, vol. 73, no. 1, pp. 17–48, 2023, doi: 10.3322/caac.21763.

[14] H. Zhou, X. Du, and Z. Zhang, "Electrochemical sensors for detection of markers on tumor cells," *Int. J. Mol. Sci.*, vol. 22, no. 15, 2021, Art. no. 8184, doi: 10.3390/ijms22158184.

[15] X. R. Li and Y. G. Zhou, "Electrochemical detection of circulating tumor cells: A mini review," *Electrochem. Commun.*, vol. 124, 2021, Art. no. 106949, doi: 10.1016/j.elecom.2021.106949.

[16] M. Y. Azab, M. F. O. Hameed, and S. S. A. Obayya, "Overview of optical biosensors for early cancer detection: Fundamentals, applications and future perspectives," *Biology*, vol. 12, no. 2, 2023, Art. no. 232, doi: 10.3390/biology12020232.

[17] Z. Geng, X. Zhang, Z. Fan, X. Lv, and H. Chen, "A route to terahertz metamaterial biosensor integrated with microfluidics for liver cancer biomarker testing in early stage," *Sci. Rep.*, vol. 7, pp. 1–11, 2017, doi: 10.1038/s41598-017-16762-y.

[18] S. Banerjee, U. Nath, P. Dutta, A. V. Jha, B. Appasani, and N. Bizon, "A theoretical terahertz metamaterial absorber structure with a high quality factor using two circular ring resonators for biomedical sensing," *Inventions*, vol. 6, no. 4, Dec. 2021, Art. no. 78, doi: 10.3390/inventions6040078.

[19] Z. Vafapour, W. Troy, and A. Rashidi, "Colon cancer detection by designing and analytical evaluation of a water-based THz metamaterial perfect absorber," *IEEE Sensors J.*, vol. 21, no. 17, pp. 19307–19313, Sep. 2021, doi: 10.1109/JSEN.2021.3087953.

[20] S. K. Patel, J. Surve, and J. Parmar, "Detection of cancer with graphene metasurface-based highly efficient sensors," *Diamond Related Mater.*, vol. 129, 2022, Art. no. 109367, doi: 10.1016/j.diamond.2022.109367.

[21] M. A. Baqir and P. K. Choudhury, "Hyperbolic metamaterial-based optical biosensor for detecting cancer cells," *IEEE Photon. Technol. Lett.*, vol. 35, no. 4, pp. 183–186, Feb. 2023, doi: 10.1109/LPT.2022.3228943.

[22] B. Amini and Z. Atlasbaf, "Design and analysis of high -sensitivity tunable graphene sensors for cancer detection," *Opt. Quantum Electron.*, vol. 55, no. 5, pp. 1–17, 2023, doi: 10.1007/s11082-023-04679-y.

[23] M. Askari, H. Pakarzadeh, and F. Shokrgozar, "High Q-factor terahertz metamaterial for superior refractive index sensing," *J. Opt. Soc. Amer. B*, vol. 38, no. 12, pp. 3929–3936, 2021, doi: 10.1364/JOSAB.438773.

[24] M. A. Z. F. H. Pakarzadeh, "Design proposal for highly sensitive infrared metamaterial-based sensors," *Opt. Quantum Electron.*, vol. 54, no. 11, pp. 1–14, 2022, doi: 10.1007/s11082-022-04143-3.

[25] R. Bhati and A. K. Malik, "Results in optics ultra-efficient terahertz metamaterial sensor," *Results Opt.*, vol. 8, 2022, Art. no. 100236, doi: 10.1016/j.rio.2022.100236.

[26] S. Ma, P. Zhang, X. Mi, and H. Zhao, "Highly sensitive terahertz sensor based on graphene metamaterial absorber," *Opt. Commun.*, vol. 528, 2023, Art. no. 129021, doi: 10.1016/j.optcom.2022.129021.

[27] P. Upender and A. Kumar, "THz dielectric metamaterial sensor with high Q for biosensing applications," *IEEE Sensors J.*, vol. 23, no. 6, pp. 5737–5744, Mar. 2023, doi: 10.1109/JSEN.2023.3239669.

[28] S. Anwar, Q. Khan, G. Ali, M. Khan, and M. Maqbool, "Triple-band terahertz metamaterial absorber with enhanced sensing capabilities," *Eur. Phys. J. D*, vol. 77, no. 4, 2023, Art. no. 69, doi: 10.1140/epjd/s10053-023-00658-w.

[29] Y. Wang, Y. Qiu, Y. Zhang, T. Lang, and F. Zhu, "High-sensitivity temperature sensor based on the perfect metamaterial absorber in the terahertz band," *Photonics*, vol. 10, no. 1, Jan. 2023, Art. no. 92, doi: 10.3390/photonics10010092.

[30] G. Li and X. Yang, "Ultra-sensitive terahertz sensing based on Rayleigh anomaly in hyperbolic metamaterial gratings," *J. Phys. D Appl. Phys.*, vol. 56, no. 5, 2023, Art. no. 55103, doi: 10.1088/1361-6463/acae32.

[31] D. Xie et al., "Terahertz metamaterial biosensor with double resonant frequencies for specific detection of early-stage hepatocellular carcinoma," *IEEE Sensors J.*, vol. 23, no. 2, pp. 1124–1131, Jan. 2023, doi: 10.1109/JSEN.2022.3225344.

[32] A. Rahman, *Finite Element Modeling Methods for Photonics*. Norwood, MA, USA: Artech House, 2013.

[33] COMSOL Multiphysics, 2018. [Online]. Available: https://www.comsol.com

[34] J. Wang, T. Lang, Z. Hong, M. Xiao, and J. Yu, "Design and fabrication of a triple-band terahertz metamaterial absorber," *Nanomaterials*, vol. 11, no. 5, pp. 1–13, 2021, doi: 10.3390/nano11051110.

[35] A. D. Squires et al., "Electrically tuneable terahertz metasurface enabled by a graphene/gold bilayer structure," *Commun. Mater.*, vol. 3, no. 1, 2022, Art. no. 56, doi: 10.1038/s43246-022-00279-7.

[36] G. Choi et al., "Terahertz conductivity of high-quality indium films deposited using a substrate cooling method," *Curr. Appl. Phys.*, vol. 52, pp. 80–84, 2023, doi: 10.1016/j.cap.2023.05.004.

[37] K. Takano, B. Kang, Y. Tadokoro, K. Kato, M. Nakajima, and M. Hangyo, *Development and Applications of Metasurfaces for Terahertz Waves BT - Electromagnetic Metamaterials: Modern Insights Into Macroscopic Electromagnetic Fields*, K. Sakoda, Ed. Berlin, Germany: Springer, 2019, pp. 99–116, doi: 10.1007/978-981-13-8649-7_7.

[38] S. Anwar and M. Khan, "Simple design of metamaterial sensor for biomedical sensing," *Phys. Scripta*, vol. 97, no. 12, 2022, Art. no. 125504, doi: 10.1088/1402-4896/ac9a87.

[39] Y. Zhan, H. Yin, J. Wang, H. Yao, and C. Fan, "Results in optics tunable multiple band THz perfect absorber with InSb metamaterial for enhanced sensing application," *Results Opt.*, vol. 8, 2022, Art. no. 100255, doi: 10.1016/j.rio.2022.100255.

[40] S. Anwar et al., "Six band terahertz absorption in metamaterial for designing optical filters, and sensors," *Opt. Quantum Electron.*, vol. 54, no. 7, 2022, Art. no. 436, doi: 10.1007/s11082-022-03821-6.

[41] L. Huang et al., "Impact of resonator geometry and its coupling with ground plane on ultrathin metamaterial perfect absorbers," *Appl. Phys. Lett.*, vol. 101, no. 10, Sep. 2012, Art. no. 101102, doi: 10.1063/1.4749823.

[42] M. Askari et al., "Additive manufacturing of metamaterials: A review," *Additive Manuf.*, vol. 36, 2020, Art. no. 101562, doi: 10.1016/j.addma.2020.101562.

[43] Y. Bai, L. Zhao, D. Ju, Y. Jiang, and L. Liu, "Band infrared perfect absorber based on L- shaped metamaterial," *Opt. Exp.*, vol. 23, no. 7, pp. 11039–11044, 2015, doi: 10.1364/OE.23.008670.

[44] H. Tao, N. I. Landy, C. M. Bingham, X. Zhang, R. D. Averitt, and W. J. Padilla, "A metamaterial absorber for the terahertz regime: Design, fabrication and characterization," *Opt. Exp.*, vol. 16, no. 10, pp. 7181–7188, 2008, doi: 10.1364/OE.16.007181.

[45] H. Tao et al., "Highly flexible wide angle of incidence terahertz metamaterial absorber: Design, fabrication, and characterization," *Phys. Rev. B*, vol. 78, no. 24, 2008, Art. no. 241103, doi: 10.1103/PhysRevB.78.241103.

[46] T. Lin et al., "Field manipulation of electromagnetically induced transparency analogue in terahertz metamaterials for enhancing liquid sensing," *Opt. Lasers Eng.*, vol. 157, 2022, Art. no. 107127, doi: 10.1016/j.optlaseng.2022.107127.

[47] J. Liu et al., "Wafer-scale metamaterials for polarization-insensitive and dual-band perfect absorption," *Nanoscale*, vol. 7, no. 45, pp. 18914–18917, 2015, doi: 10.1039/C5NR05479F.

[48] J. Wang, T. Lang, Z. Hong, T. Shen, and G. Wang, "Tunable terahertz metamaterial absorber based on electricity and light modulation modes," *Opt. Mater. Exp.*, vol. 10, no. 9, pp. 2262–2273, 2020, doi: 10.1364/ome.402541.

[49] H. Jing et al., "Thermally and magnetically controlled dual-band terahertz metamaterial absorber based on InSb," *Opt. Mater.*, vol. 129, 2022, Art. no. 112311, doi: 10.1016/j.optmat.2022.112311.

[50] M. Salman, S. I. M. Kotb, G. H. Mohammed, M. El Okr, S. S. A. Obayya, and M. F. O. Hameed, "Highly sensitive photonic crystal gamma ray dosimeter," *Opt. Quantum Electron.*, vol. 53, no. 7, pp. 1–19, 2021, doi: 10.1007/s11082-021-02968-y.

[51] P. Agarwal, K. Kishor, and R. K. Sinha, "Ultrasensitive dual-band terahertz metasurface sensor based on all InSb resonator," *Opt. Commun.*, vol. 522, 2022, Art. no. 128667, doi: 10.1016/j.optcom.2022.128667.

[52] N. Liu and H. Giessen, "Coupling effects in optical metamaterials," *Angewandte Chemie Int. Ed.*, vol. 49, no. 51, pp. 9838–99852, 2010, doi: 10.1002/anie.200906211.

[53] M.-R. Nickpay, M. Danaie, and A. Shahzadi, "Design of a graphene-based multi-band metamaterial perfect absorber in THz frequency region for refractive index sensing," *Phys. E Low-Dimensional Syst. Nanostructures*, vol. 138, 2022, Art. no. 115114, doi: 10.1016/j.physe.2021.115114.

[54] M. Zhong, "Measurement and verification of a multi-band terahertz metamaterial absorber based on multiple coupling effects," *Infrared Phys. Technol.*, vol. 128, 2023, Art. no. 104506, doi: 10.1016/j.infrared.2022.104506.

[55] B. X. Wang, X. Zhai, G. Z. Wang, W. Q. Huang, and L. L. Wang, "A novel dual-band terahertz metamaterial absorber for a sensor application," *J. Appl. Phys.*, vol. 117, 2015, doi: 10.1063/1.4905261.

[56] P. Jain et al., "Machine learning assisted hepta band THz metamaterial absorber for biomedical applications," *Sci. Rep.*, vol. 13, no. 1, 2023, Art. no. 1792, doi: 10.1038/s41598-023-29024-x.

[57] Z. Dai et al., "Tracing pictogram-level chlorothalonil pesticide based on terahertz metal–graphene hybrid metasensors," *Opt. Commun.*, vol. 529, 2023, Art. no. 129025, doi: 10.1016/j.optcom.2022.129025.

[58] H. Ge et al., "Design of high-performance terahertz sensor based on metamaterials," *J. Phys. Conf. Ser.*, vol. 2174, no. 1, 2022, Art. no. 12001, doi: 10.1088/1742-6596/2174/1/012001.

[59] S. K. Koul and P. Kaurav, *Sub-Terahertz and Terahertz Waves for Skin Diagnosis and Therapy in: Sub-Terahertz Sensing Technology for Biomedical Applications*. Berlin, Germany: Springer, 2022, doi: 10.1007/978-981-19-3140-6.

[60] A. J. Fitzgerald, E. Pickwell-MacPherson, and V. P. Wallace, "Use of finite difference time domain simulations and debye theory for modelling the terahertz reflection response of normal and tumour breast tissue," *PLoS One*, vol. 9, no. 7, 2014, Art. no. e99291, doi: 10.1371/journal.pone.0099291.

[61] M. El-Shenawee, N. Vohra, T. Bowman, and K. Bailey, "Cancer detection in excised breast tumors using terahertz imaging and spectroscopy," *Biomed. Spectrosc. Imag.*, vol. 8, no. 1/2, pp. 1–9, 2019, doi: 10.3233/bsi-190187.

[62] K. Chen, "Ultra-sensitive terahertz metamaterials biosensor based on luxuriant gaps structure," *Iscience*, vol. 26, no. 1, 2023, Art. no. 105781, doi: 10.1016/j.isci.2022.105781.

[63] Y. Shen et al., "Low-concentration biological sample detection using an asymmetric split resonator terahertz metamaterial," *Photonics*, vol. 10, no. 2, Jan. 2023, Art. no. 111, doi: 10.3390/photonics10020111.

[64] Z. Mezache, Z. Hafdi, and J. Tao, "Design of a novel graphene buzzle metamaterial refractometer for sensing of cancerous cells in the terahertz regime," *Optik*, vol. 287, 2023, Art. no. 171170, doi: 10.1016/j.ijleo.2023.171170.

[65] D. Liang and T. Chen, "Optical modulated graphene metamaterial based on plasmon-induced transparency in the terahertz band: Application for sensing," *Diamond Related Mater.*, vol. 131, 2023, Art. no. 109613, doi: 10.1016/j.diamond.2022.109613.

[66] Y. Cheng, Y. Qian, H. Luo, F. Chen, and Z. Cheng, "Terahertz narrowband perfect metasurface absorber based on micro-ring-shaped GaAs array for enhanced refractive index sensing," *Phys. E Low-Dimensional Syst. Nanostructures*, vol. 146, 2023, Art. no. 115527, doi: 10.1016/j.physe.2022.115527.

[67] H. E. Nejad, A. Mir, and A. Farmani, "Supersensitive and tunable nano-biosensor for cancer detection," *IEEE Sensors J.*, vol. 19, no. 13, pp. 4874–4881, Jul. 2019, doi: 10.1109/JSEN.2019.2899886.

[68] D. Li et al., "Identification of early-stage cervical cancer tissue using metamaterial terahertz biosensor with two resonant absorption frequencies," *IEEE J. Sel. Topics Quantum Electron.*, vol. 27, no. 4, Jul./Aug. 2021, Art. no. 8600107, doi: 10.1109/JSTQE.2021.3058163.

[69] S. Anwar and M. Khan, "High-performance terahertz refractive index sensor for cancer cells detection," *Eur. Phys. J. E*, vol. 46, no. 3, 2023, Art. no. 19, doi: 10.1140/epje/s10189-023-00274-x.